Spatiotemporal Forecasting of Pine Wilt Disease in China Using a Graph Convolutional-LSTM Network

Xuanli He, Yingying Dong, Zhuoqing Hao, Wenjiang Huang, Biyao Zhang, Jing Guo, Yan Zhang, Minghao Wang, Tonghui Qi, and Guofei Fang

***Abstract*—The escalating spread of pine wilt disease (PWD) presents a severe threat to forest ecosystems, while predicting its complex spatiotemporal dynamics remains a major challenge. To address this, we developed a novel deep learning framework integrating a graph convolutional network (GCN) with a long short-term memory (LSTM) network to deconstruct and predict the occurrence of PWD (OPWD) in China for the period 1982–2022. Using GeoDetector, we identified 16 key factors and quantified their contributions, revealing that human-mediated factors (e.g., wood-processing factory density and road network density) are the dominant drivers of PWD spread, exhibiting strong synergistic interactions. The GCN-LSTM model demonstrated exceptional predictive performance, significantly outperforming conventional models with an overall accuracy of 0.93 and an AUC of 0.87. Crucially, the model deconstructed the spread of PWD into two distinct mechanisms: a stable, localized, continuous spread governed by natural factors; and a volatile, long-distance leaping spread driven primarily by human activities. This mechanistic deconstruction provides a robust explanation for the historical patterns of the epidemic. This study provides not only a highly accurate predictive tool for large-scale PWD monitoring but also a powerful analytical paradigm for disentangling the drivers of biological invasions, underscoring the imperative for developing spatially explicit, mechanism-aware management strategies to effectively combat the global threat of PWD.**

***Index Terms*—GeoDetector, graph convolutional network (GCN), long short-term memory (LSTM), pine wilt disease (PWD), spatiotemporal prediction.**

I. Introduction

PINE wilt disease (PWD) is a lethal forest disease caused by the pine wood nematode (PWN, *Bursaphelenchus xylophilus*) that induces wilting, yellowing, and browning of needles within approximately three months, ultimately resulting in tree mortality. This rapid pathology has earned it the moniker "pine cancer" in forestry literature [1], [2]. Originating in North America, PWD has become a global concern, with significant infestations reported across China, Japan, South Korea, Portugal, and Spain. China has been listed as the most vulnerable country against this disease [3]. Since its 1982 detection at Nanjing's Sun Yat-sen Mausoleum [4], [5], PWD has expanded across 18 Chinese provinces by 2024 and incurred up to 20 billion RMB in economic losses according to the statistics of the Chinese National Forestry Bureau [5], [6], [7]. This accelerating spread, compounded by limited containment options [8], triggers severe ecological degradation, including diminished carbon sequestration, accelerated soil erosion, and biodiversity loss within ecosystems [9], [10].

The expansion risk of invasive species is fundamentally linked to their dispersal capacity [11], which for PWD manifests through two distinct yet interacting spatial processes: continuous and leaping spread [12], [13]. The first process, natural continuous spread, generates a gradual, wave-like expansion from infection foci. This spread is strongly constrained by a well-defined environmental niche. Key biophysical drivers include climatic factors, such as temperature regimes and precipitation patterns, which modulate host tree stress and vector beetle activity [3], [14], [15], [16]. Topography also plays a critical role, with low-elevation areas creating favorable microclimates that increase habitat suitability and disease vulnerability [14], [17], [18]. These environmental controls define the fundamental geographic boundaries for the establishment of PWD.

However, the observed rapid, long-distance expansion of PWD frequently transcends these natural environmental thresholds, driven by a second process: human-mediated leaping spread. Human activity is a primary vector for introducing the pathogen into new, often environmentally suitable regions,

Received 22 September 2025; revised 25 December 2025; accepted 28 January 2026. Date of publication 11 February 2026; date of current version 5 March 2026. This work was supported in part by the National Natural Science Foundation of China under Grant 42201355; in part by the Research on Remote Sensing Monitoring of Crop Growth and Disease and Pest under the Background of Climate Change under Grant E44702010T; in part by the Sino-UK Crop Pest and Disease Forecasting and Management Joint Laboratory under Grant 183611ZYLH20240009; in part by the Sino-EU Dragon 6 Proposal: Optical and Thermal Copernicus—Chinese Eodata for Analyzing the Driving Factors, Impacting on Food Security and Quality under Grant 95250; and in part by the GEO-PDRS: Global Vegetation Pest and Disease Dynamic Remote Sensing Monitoring and Forecasting. *(Corresponding author: Yingying Dong.)*

Xuanli He, Yingying Dong, Wenjiang Huang, Jing Guo, Yan Zhang, and Minghao Wang are with the State Key Laboratory of Remote Sensing and Digital Earth, Aerospace Information Research Institute, Chinese Academy of Sciences, Beijing 100094, China, and also with the University of Chinese Academy of Sciences, Beijing 100049, China (e-mail: dongyy@aircas.ac.cn).

Zhuoqing Hao, Biyao Zhang, and Tonghui Qi are with the State Key Laboratory of Remote Sensing and Digital Earth, Aerospace Information Research Institute, Chinese Academy of Sciences, Beijing 100094, China.

Guofei Fang is with the Center for Biological Disaster Prevention and Control, National Forestry and Grassland Administration, Shenyang 110034, China, and also with the Key Laboratory of National Forestry and Grassland Administration on Forest and Grassland Pest Monitoring and Warning, Shenyang 110034, China.

This article has supplementary downloadable material available at https://doi.org/10.1109/TGRS.2026.3663660, provided by the authors.

Digital Object Identifier 10.1109/TGRS.2026.3663660

1558-0644 © 2026 IEEE. All rights reserved, including rights for text and data mining, and training of artificial intelligence and similar technologies. Personal use is permitted, but republication/redistribution requires IEEE permission.
See https://www.ieee.org/publications/rights/index.html for more information.

Authorized licensed use limited to: University of Chinese Academy of SciencesCAS. Downloaded on March 10,2026 at 08:18:33 UTC from IEEE Xplore. Restrictions apply.

thereby initiating multipoint outbreaks and complicating predictive modeling and control efforts. This leaping spread, facilitated by the transport of infested materials like timber and wood packaging, can dramatically accelerate the disease's range expansion far beyond the front of a continuous traveling wave [19], [20], [21]. For instance, Pukkala et al. [22] found that higher human population density and frequent timber entries from major ports corresponded to increased PWD risk in regions of Finland and Iberia. In China's Yangtze River Basin, spatiotemporal scan statistics revealed "jumping propagation: multipoint outbreak" patterns closely linked to transportation corridors and urban agglomerations, underscoring the role of human facilitation in leaping spread [23].

A range of modeling techniques has been deployed to forecast the spread and prevalence of PWD, among which, prediction models demonstrating robust performance and broad adoption fall into two primary categories: species distribution models (SDMs) and process-based models. SDMs, particularly MaxEnt and ensemble techniques, leverage biophysical variables (e.g., climatic, topographic, soil) to geographically delineate habitat suitability through occurrence-environment correlations and have consistently demonstrated high predictive performance in mapping current risk [14], [16]. Predictions of future risk under climate change using these models forecast significant poleward range expansion into previously unsuitable high-latitude regions [24], [25]. However, they are often static or quasi-static, struggling to explicitly represent the mechanisms and temporal sequencing of the spread process itself. Process-based and dynamic epidemiological models have complemented correlative SDMs. Hao et al. [26] integrated susceptible–infectious–susceptible (SIS) and random forest (RF) models to simulate continuous and leapfrog spread over 40 years, demonstrating that combined modeling can effectively reconstruct historical dissemination patterns. In Anhui Province, a cellular automata–Markov (CA–Markov) model has produced robust results, achieving 93% overall accuracy, 95% grid accuracy, and a kappa coefficient of 0.65 in predicting PWD distribution for 2030 [18]. European applications further demonstrated CA models' sensitivity to temperature gradients and anthropogenic pathways [22].

Predicting the occurrence of PWD (OPWD) is essential for proactive management, as postinfestation control is cost-prohibitive [10], [27], [28]. However, unifying stochastic leaping spread and continuous dispersal within intrinsic spatiotemporal structures remains challenging [29]. We address this by proposing a framework that explicitly models the spatiotemporal dependencies of OPWD. By coupling GeoDetector with an enhanced graph convolutional network (GCN)-LSTM architecture, this study provides three key innovations: 1) a dual-graph structure representing natural and anthropogenic transmission pathways; 2) a mechanistic decomposition of invasion processes into quantifiable continuous and leaping spread; and 3) a hybrid approach integrating deep learning with statistical driver analysis to enhance interpretability.

Validated against 40-year historical records in China (1982–2022), the framework yields high-resolution risk maps and elucidates evolving driver roles. Beyond forecasting, this research presents a robust paradigm for disentangling the complex interactions of biological invasions. The model's ability to handle multifaceted ecological and anthropogenic factors provides a mechanistic understanding of their interplay. These spatially explicit insights offer critical guidance for forestry agencies to implement targeted biosecurity and resource-efficient management, providing a scientific foundation for mitigating invasive species threats in an increasingly interconnected world.

TABLE I
TYPES OF INTERACTION BETWEEN TWO FACTORS

Condition	Type of Interaction
$q(X_1 \cap X_2) < \min(q(X_1), q(X_2))$	Weaken, nonlinear
$\min(q(X_1), q(X_2)) < q(X_1 \cap X_2) < \max(q(X_1), q(X_2))$	Weaken, uni-
$q(X_1 \cap X_2) > \max(q(X_1), q(X_2))$	Enhance, bi-
$q(X_1 \cap X_2) = q(X_1) + q(X_2)$	Independent
$q(X_1 \cap X_2) > q(X_1) + q(X_2)$	Enhance, nonlinear

II. STUDY AREA AND DATA

A. Study Area

This study focuses on mainland China, a vast territory extending from 21°N to 53°N and 73°E to 135°E. The country's geography encompasses a wide gradient of climatic zones, including subtropical, temperate, and alpine regions, which collectively support diverse and extensive pine ecosystems. These pine forests are critical national resources, constituting over 23% of China's total forest cover [30].

The prevalence of pine forests creates a susceptible landscape for the establishment and spread of PWD. In China, at least 17 native tree species are vulnerable to PWN infection, with the most susceptible primary hosts being *Pinus densiflora*, *Pinus thunbergii*, and *Pinus massoniana* [31]. Recent climatic-habitat suitability analyses confirm that the majority of China's territory provides favorable conditions for PWN survival [32]. Coupled with the high adaptability of PWN, the disease has expanded beyond its historical range, posing a significant threat to nearly all pine-forested counties nationwide [31]. This long-term, large-scale invasion, as shown in Fig. 1, marked by long-distance dispersal and rapid spread, makes China an ideal natural laboratory for analyzing the spatiotemporal dynamics of a major forest pandemic.

B. Data

Based on preliminary research, we collected remote sensing data, ground survey records, and other auxiliary data for this study. After preprocessing, 42 influencing factors potentially impacting the OPWD were prepared for analysis. All variables span the 40-year study period. Temporal raster data were averaged annually, while vector data were aggregated at the county scale. A detailed summary of all data sources is provided in the Supplementary Table 1, with key datasets outlined as follows.

1) Remote Sensing and Derivative Geospatial Products:

1) *Climatic and Environmental Data:* Monthly aggregated data for temperature, precipitation, snowfall, snowmelt,

Authorized licensed use limited to: University of Chinese Academy of SciencesCAS. Downloaded on March 10,2026 at 08:18:33 UTC from IEEE Xplore. Restrictions apply.

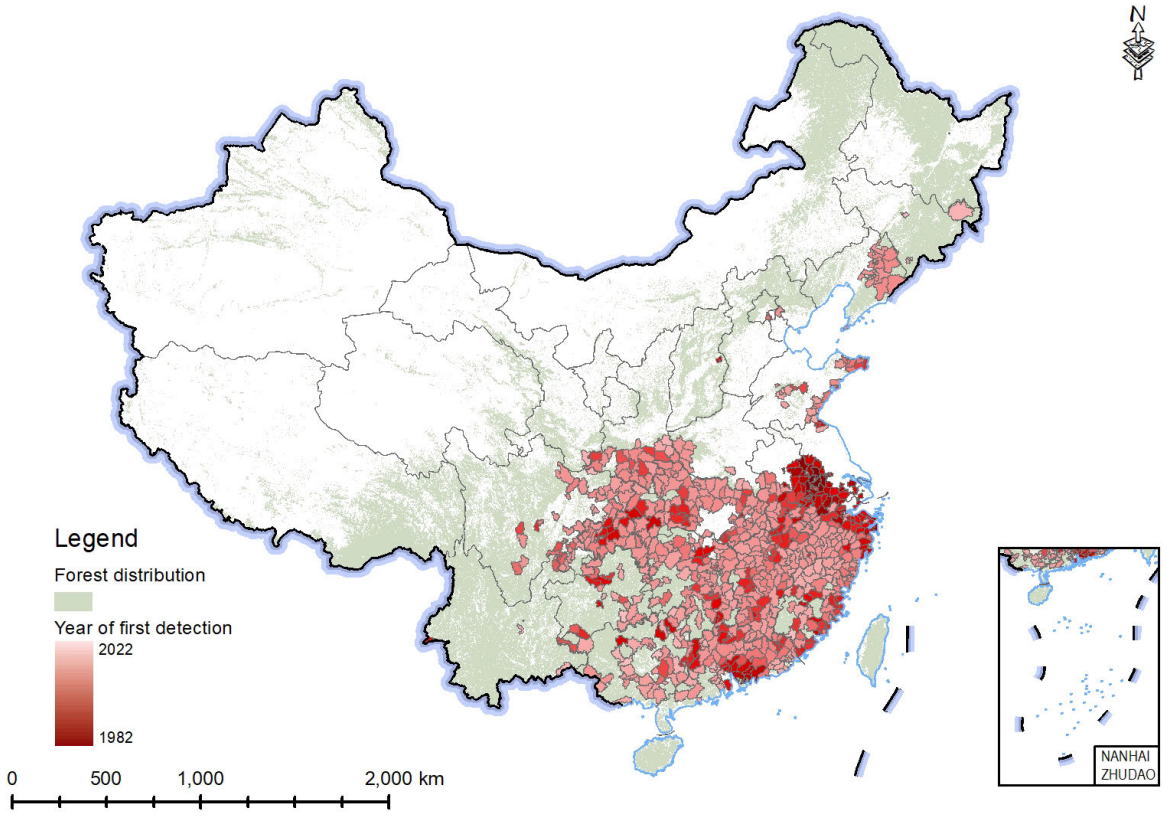


Fig. 1. Temporal evolution and spatial distribution of PWD-affected counties in China for the period 1982–2022.

evapotranspiration, solar radiation, wind speed, leaf area index, soil moisture, and surface pressure were derived from the ERA5-Land dataset (https://developers.google.com/earth-engine/datasets/catalog/ECMWF_ERA5_LAND_MONTHLY_AGGR). The Standardized Precipitation-Evapotranspiration Index (SPEI) was sourced from the SPEIbase dataset (https://developers.google.com/earth-engine/datasets/catalog/CSIC_SPEI_2_9). Both were accessed via the Google Earth Engine (GEE) platform.

2) *Soil Data:* Clay content was obtained from the OpenLandMap dataset (https://www.openlandmap.org/).
3) *Topographic Data:* Digital elevation model (DEM), topographic roughness, topographic index, slope, aspect, and mountain shadow (MS) index were computed from the Copernicus GLO-30 DEM, available at https://portal.opentopography.org/
4) *Nighttime Light Data:* A long-term, harmonized satellite product from 1984 to 2020 developed by Zhang et al. [33] was used.
5) *Land Cover Data:* The 30-m China National Land Use/Land Cover Change (CNLUCC) dataset was sourced from the Resource and Environment Science and Data Center, Chinese Academy of Sciences (RESDC) at https://www.resdc.cn/

2) Field Survey and Tabular Data:

1) *OPWD and Factory Data:* The core dataset of PWD presence/absence at the county level, along with the distribution of wood-processing factories, was provided by the National Forestry and Grassland Administration (NFGA) of China (https://www.forestry.gov.cn/). These records are based on biannual field surveys.
2) *Transportation Network:* Road network data were extracted from OpenStreetMap (https://download.geofabrik.de/asia.html), and port locations were obtained from Natural Earth (https://www.naturalearthdata.com/downloads/).
3) *Population Data:* Gridded population density was derived from the GHS-POP R2023A multitemporal (1975–2030) dataset [34].

3) Ancillary Geospatial Data:

1) *Administrative Boundaries:* Vector data of China's administrative boundaries served as the fundamental geospatial framework for aggregating all predictor and response variables.

III. Methods

A. Extraction of Influencing Factors

In this study, we employed the GeoDetector to quantify the influence of various natural and human-mediated factors on the spatial heterogeneity of OPWD. First, we calculated the q-values at the county level and retained all variables whose q-statistics ranked in the top 50% as the preliminary screening result. Different from traditional regression models, the GeoDetector is particularly well-suited for analyzing complex environmental systems as it does not require assumptions

Authorized licensed use limited to: University of Chinese Academy of SciencesCAS. Downloaded on March 10,2026 at 08:18:33 UTC from IEEE Xplore. Restrictions apply.

TABLE II
INFLUENCING FACTORS SELECTED FOR PREDICTING OPWD

Class	Name	Meaning	Unit	Range	Average	Std. Dev.
Natural factors	annual_pre	annual mean precipitation	m	[0, 0.32]	0.14	0.04
	EVT	evaporation from vegetation transpiration	m of water equivalent	[-0.06, 0]	0.00	0.00
	SoilMoi68	average summertime (June–August) soil moisture	Volume fraction	[0, 0.48]	0.39	0.06
	tem68	average summertime (June–August) temperature	K	[0, 303.53]	295.26	32.07
	wind	annual mean wind speed	m/s	[0, 3.65]	0.59	0.29
	wind68	average summertime (June–August) wind speed	m/s	[0, 3.77]	0.77	0.40
	DEM	elevation	m	[0, 2975.42]	387.64	363.82
	MS	mountain shadow index	-	[0, 181]	59.67	9.56
	forest_per	forest area percentage	%	[0, 0.93]	0.45	0.26
	con_per	construction area percentage	%	[0, 0.93]	0.07	0.12
Human-mediated factors	POP	population mobility	km^{-2}	[-4.03, 60.27]	0.48	2.00
	FPP	forest proximate population	km^{-2}	[0, 574.22]	2.67	9.45
	nightlight	nighttime-light	-	[0, 6287.89]	624.21	1084.93
	road_density	road network density	km/km^2	[0.02, 20.37]	0.94	1.54
	factory	wood-processing factory density	km^{-2}	[0, 2205]	14.09	42.01
	factory_change	change in number of wood-processing factories	-	[0, 922]	1.48	8.19

of linearity between variables [35], and it has been extensively applied in ecological and environmental research for attribution analysis [36], [37]. The fundamental premise of GeoDetector is that if a potential factor (X) significantly influences a geographic phenomenon (Y), their spatial distributions will exhibit a strong similarity [35], [38]. We utilized the factor and interaction detector modules to assess the individual and combined effects of potential influencing factors on OPWD.

Since all continuous explanatory variables must be discretized into categorical data in GeoDetector, and the classification methods can significantly impact the resulting q-statistics [39], we employed the K-means clustering algorithm to stratify each influencing factor. The optimal number of clusters was systematically determined through dual-criteria validation, integrating the silhouette coefficient evaluation and the elbow method analysis to ensure an objective and data-driven classification.

The explanatory strength of each factor X on OPWD (Y) was then expressed by the q statistic [40]

$$q = 1 - \frac{\sum_{h=1}^{L} N_h \sigma_h^2}{N\sigma^2} = 1 - \frac{\mathrm{SSW}}{\mathrm{SST}} \tag{1}$$

where SSW and SST are defined as

$$\mathrm{SSW} = \sum_{h=1}^{L} N_h \sigma_h^2 \qquad \mathrm{SST} = N\sigma^2. \tag{2}$$

Here, $h = 1, \ldots, L$ represents the strata of factor X. N_h and N are the number of sample units in stratum h and the entire study area, respectively, while σ_h^2 and σ^2 are the variances of Y within stratum h and the entire study area. SSW and SST denote the sum of within-stratum variance and the total sum of squares, respectively. The q-value ranges from 0 to 1, indicating that factor X explains $q \times 100\%$ of the OPWD. A q-value of 1 signifies that factor X completely determines the spatial distribution of Y, while a value of 0 indicates no spatial association.

Furthermore, the synergistic or antagonistic effects of paired environmental drivers (X_1 and X_2) on OPWD were assessed by the interaction detector. First, this approach quantifies the individual q-value of each factor: $q(X_1)$ and $q(X_2)$. Subsequently, the q-value representing the combined explanatory power of their interaction, denoted as $q(X_1 \cap X_2)$, was calculated. The interactive relationship between X_1 and X_2 was then categorized into one of five distinct types based on the comparative magnitudes of $q(X_1)$, $q(X_2)$, and $q(X_1 \cap X_2)$. These five categories are shown in Table I.

Following the GeoDetector analysis, a two-stage screening process was implemented to finalize the set of predictors for OPWD. First, an initial selection was made based on explanatory power, retaining all factors whose q-statistics ranked in the top 50%. Second, to mitigate multicollinearity, which can lead to model overfitting and instability, we calculated the Pearson correlation coefficients between the remaining factors [24]. For any pair of variables with a high correlation ($|R| > 0.7$), only the one with the higher q-statistic was retained, while the other was eliminated [41]. The final set of selected influencing factors used for predicting OPWD is presented in Table II.

B. GCN-LSTM-Fusion Model

1) Graph Construction: Graph construction is usually preferred to represent the spatial relationships of geospatial data. To effectively model the complex spatiotemporal dynamics of OPWD, we represent the potential transmission paths among the PWD-affected counties as a graph structure. The system at each time step t is defined as a graph signal, where the features of N counties are represented by a feature matrix $\mathbf{X}_t \in \mathbb{R}^{N \times M}$, with M being the number of features for each node. The spatial relationships are encoded in a directed graph $G = (V, E, \mathbf{A})$, where V is the set of N nodes ($v_i \in V$) representing the 817 county-level units with historical PWD outbreaks, E is the set of edges representing potential transmission pathways, and

Authorized licensed use limited to: University of Chinese Academy of SciencesCAS. Downloaded on March 10,2026 at 08:18:33 UTC from IEEE Xplore. Restrictions apply.

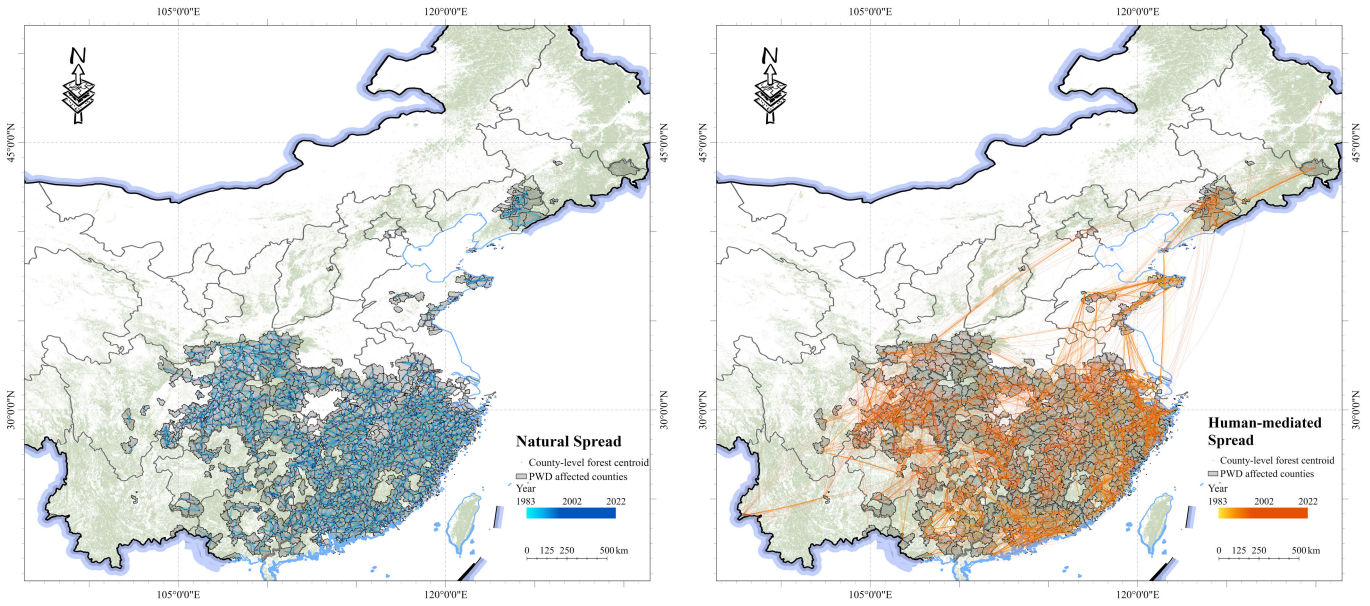


Fig. 2. (a) Natural spread network and (b) human-mediated spread network.

$\mathbf{A} \in \mathbb{R}^{N\times N}$ is the weighted adjacency matrix quantifying the strength of the spatial correlation between any two nodes v_i and v_j ($A_{ij} > 0$).

Considering the spatial uncertainty in outbreak locations, we implemented an iterative training procedure to calibrate the weight matrices. We represented the 817 county-level units with reported PWD outbreaks between 1982 and 2022 as graph nodes, each anchored to the centroid of its forested area rather than its administrative center and characterized by the environmental and socioeconomic covariates described above. Within this framework, two complementary adjacency matrices were constructed to model the dual propagation mechanisms of PWD (see Fig. 2). To represent continuous spread facilitated by vector insects, a natural spread network was constructed based on the spatial adjacency and geographic proximity of forest distributions, thereby linking counties with contiguous or proximal susceptible habitats. Concurrently, to capture long-distance leaping spread-driven by anthropogenic activities, a human-mediated spread network was inferred using a source-sink paradigm. In this network, regions with an increasing density of wood-processing factories were designated as potential sources, while those with expanding construction land, which is a proxy for timber demand, were identified as sinks, with the connecting paths constructed based on road connectivity.

2) Spatial Dependency Modeling: To model the complex, non-Euclidean spatial dependencies inherent in the PWD transmission network, we implemented a GCN framework grounded in spectral graph convolution, which generalizes the concept of traditional convolution to graph-structured data by operating in the graph Fourier domain. Intuitively, this can be understood as extending the idea of filtering signals on regular grids (like images) to irregular graph structures, where nodes represent counties and edges represent potential transmission pathways between them. This operation is fundamentally governed by the graph's topology, which is mathematically encoded in the normalized graph Laplacian matrix, $\mathbf{L}$ [42]. The graph Laplacian quantifies how different a node's features are from its neighbors, effectively capturing the smoothness of signal variation across the network. The Laplacian is derived from the graph's adjacency matrix $\mathbf{A}$ and diagonal degree matrix $\mathbf{D}$ as

$$\mathbf{L} = \mathbf{I}_N - \mathbf{D}^{-1/2}\mathbf{A}\mathbf{D}^{-1/2} = \mathbf{U}\mathbf{\Lambda}\mathbf{U}^T. \tag{3}$$

Here, $\mathbf{I}_N$ is the identity matrix, and the eigendecomposition of $\mathbf{L}$ yields a matrix of eigenvectors $\mathbf{U}$ and a diagonal matrix of eigenvalues $\mathbf{\Lambda}$.

The spectral convolution of a graph signal $\mathbf{x}$ (representing node features) with a learnable filter g_θ can be expressed as the multiplication of the filter and the signal in the Fourier domain. This operation is defined as

$$\mathbf{y} = g_\theta * \mathbf{x} = g_\theta(\mathbf{L})\,\mathbf{x} = g_\theta\left(\mathbf{U}\mathbf{\Lambda}\mathbf{U}^T\right)\mathbf{x} = \mathbf{U}g_\theta(\mathbf{\Lambda})\,\mathbf{U}^T\mathbf{x} \tag{4}$$

where $\mathbf{U}^T\mathbf{x}$ constitutes the graph Fourier transform of the signal, and $g_\theta(\mathbf{\Lambda})$ is a function of Laplacian's eigenvalues, parameterized by a vector of learnable coefficients θ.

To enhance computational efficiency, we adopted a truncated Chebyshev polynomial expansion of $g_\theta(\mathbf{\Lambda})$, which reduces complexity while preserving spectral filtering capabilities. This approach further generalizes the graph convolution defined in (4) to accommodate spatiotemporal feature matrices $\mathbf{X}_t \in \mathbb{R}^{N\times M}$ and multifilter weight tensors [43] as

$$\mathbf{H} = \sum_{k=0}^{K} T_k\left(\tilde{\mathbf{L}}\right)\mathbf{X}_t\mathbf{\Theta}_k \tag{5}$$

where $\mathbf{H} \in \mathbb{R}^{N\times W}$ represents the convolved spatial feature matrix, $\mathbf{\Theta}_k \in \mathbb{R}^{M\times W}$ is a matrix of learnable filter parameters, and $T_k(\tilde{\mathbf{L}})$ is the Chebyshev polynomial of order k applied to the scaled Laplacian $\tilde{\mathbf{L}} = 2\mathbf{L}/\lambda_{\max} - \mathbf{I}_N$, where $\lambda_{\max}$ is the largest eigenvalue of $\mathbf{L}$.

Authorized licensed use limited to: University of Chinese Academy of SciencesCAS. Downloaded on March 10,2026 at 08:18:33 UTC from IEEE Xplore. Restrictions apply.

We modeled distinct diffusion scales of PWD using K-hop graph convolutions, where Kth-order filtering restricts feature aggregation to nodes within K-hop neighborhoods [44]. A 1-hop convolution ($K = 1$) captured a continuous spread by restricting influence to immediate neighbors. Conversely, a 2-hop convolution ($K = 2$) simulated leaping spread by modeling a long-distance introduction and its subsequent secondary diffusion.

3) Temporal Dependency Modeling: The temporal dimension of PWD outbreaks, evident in the time-series nature of historical monitoring data, necessitates a modeling approach capable of capturing sequential dependencies. This study employs the long short-term memory (LSTM) network, which is derived from recurrent neural networks (RNNs) but overcomes the limitations of vanishing and exploding gradients, making it adept at learning long-range temporal dependencies [45].

The core of the chain-structured LSTM is a memory cell, whose information flow is regulated by three gating mechanisms: a forget gate f_t, an input gate i_t, and an output gate o_t. These gates, composed of sigmoid-activated neural network layers, dynamically control the retention, storage, and exposure of information within the cell state C_t. The state transitions and information flow at each time step t are governed by the following equations:

$$f_t = \sigma\left(\mathbf{W}_f \cdot [h_{t-1}, x_t] + b_f\right) \tag{6}$$

$$i_t = \sigma\left(\mathbf{W}_i \cdot [h_{t-1}, x_t] + b_i\right) \tag{7}$$

$$\tilde{C}_t = \tanh\left(\mathbf{W}_c \cdot [h_{t-1}, x_t] + b_c\right) \tag{8}$$

$$C_t = f_t \circ C_{t-1} + i_t \circ \tilde{C}_t \tag{9}$$

$$o_t = \sigma\left(\mathbf{W}_o \cdot [h_{t-1}, x_t] + b_o\right) \tag{10}$$

$$h_t = o_t \circ \tanh\left(C_t\right). \tag{11}$$

Here, σ and tanh denote the sigmoid and hyperbolic tangent activation functions, respectively. x_t is the input at the current time step, and h_{t-1} is the hidden state from the previous step. The terms $\mathbf{W}$ and b represent the learnable weight matrices and bias vectors for each respective gate and cell update calculation. The symbol $\circ$ denotes the Hadamard (elementwise) product, and the square brackets $[\cdot]$ represent the concatenation of vectors.

In addition, to avoid the gradient explosion problem, gradient clipping was used with a threshold value of 2, ensuring that the norm of the gradients ∇ did not exceed this threshold during the model update

$$\text{Clipped } \nabla = \nabla \cdot \max\left(2, \frac{threshold}{\|\nabla\|}\right). \tag{12}$$

4) Spatiotemporal Prediction Architecture: To effectively model the complex transmission dynamics of PWD, we developed a hybrid deep learning architecture that integrates a GCN with an LSTM network. The primary objective of this GCN-LSTM model is to forecast the future OPWD by learning from historical spatiotemporal patterns. As illustrated in (see Fig. 3), the proposed architecture is explicitly designed not only for prediction but also to provide insights into the underlying mechanisms, thereby enhancing model interpretability. The prediction task is formally defined as learning a mapping function $h(\cdot)$ that uses a sequence of observations over a preceding time window of size T to predict future PWD status. Given a graph $G = (V, E, \mathbf{A})$, the model predicts the PWD occurrence sequence $[\widehat{\text{OPWD}}_{(t+1)}, \ldots, \widehat{\text{OPWD}}_{(t+T')}]$ based on input features $[\mathbf{x}_{t-T+1}, \ldots, \mathbf{x}_t]$. This can be expressed as

$$\left[\widehat{\text{OPWD}}(t+1), \ldots, \widehat{\text{OPWD}}\left(t+T'\right)\right] = h\left(\left[\mathbf{x}_{t-T+1}, \ldots, \mathbf{x}_t\right]; G\left(V, E, A\right)\right). \tag{13}$$

In our implementation, we adopted a rolling prediction scheme for sequential, one-step-ahead forecasting ($T' = 1$), where the model is trained to find the pattern between the PWD status at time t_i and its n preceding values. The temporal window size was empirically determined to be $n = 5$.

The architecture of our proposed GCN-LSTM model, as illustrated in Fig. 3, employs a multistage process. In the first stage, a GCN module is utilized for spatial feature extraction. At each time step t, the GCN operates on the node feature matrix $\mathbf{X}_t$ and the adjacency matrix $\mathbf{A}$ to generate a spatially aware hidden representation $\mathbf{H}_t$. In the second stage, these learned spatial features $\mathbf{H}_t$ are concatenated with the original input signals $\mathbf{X}_t$ to form an enriched input for the LSTM ($\mathbf{X}_t^{\text{GCN}}$). The final hidden state from the LSTM is then passed to a fully connected (FC) layer. Consequently, the FC layer maps the high-dimensional features to two separate output logits, which are transformed into probabilities via a sigmoid activation function. These probabilities represent the continuous spread probability (CSP) and leaping spread probability (LSP), respectively. The final binary classification of OPWD is determined through a threshold-based fusion strategy.

The model was trained end-to-end using the AdamW optimizer to minimize a numerically stable binary cross-entropy loss (BCEWithLogitsLoss). A cosine annealing scheduler with warm restarts was employed to dynamically adjust the learning rate. To prevent overfitting, we implemented dropout regularization following the GCN and LSTM layers, complemented by the decoupled weight decay inherent to AdamW. Optimal hyperparameters were determined through a systematic search using the Optuna framework. A total of 50 Bayesian optimization trials were performed with the objective of maximizing the area under the receiver operating characteristic curve (ROC AUC) [17]. This process tuned key parameters, including hidden dimensions, learning rate, dropout rate, and weight decay, and conducted a maximum of 200 epochs of model-training to ensure stable parameter convergence.

C. Evaluation Indicators

The performance of the GCN-LSTM model was rigorously evaluated by comparing its predictions against ground-truth PWD incidence data. The final binary predictions were assessed using a standard confusion matrix, which categorizes outcomes into four types: true positives (TP, correctly identified PWD occurrences); false positives (FP, PWD predicted but not present); true negatives (TN, correctly identified nonoccurrences); and false negatives (FN, an actual PWD occurrence missed by the model).

Authorized licensed use limited to: University of Chinese Academy of SciencesCAS. Downloaded on March 10,2026 at 08:18:33 UTC from IEEE Xplore. Restrictions apply.

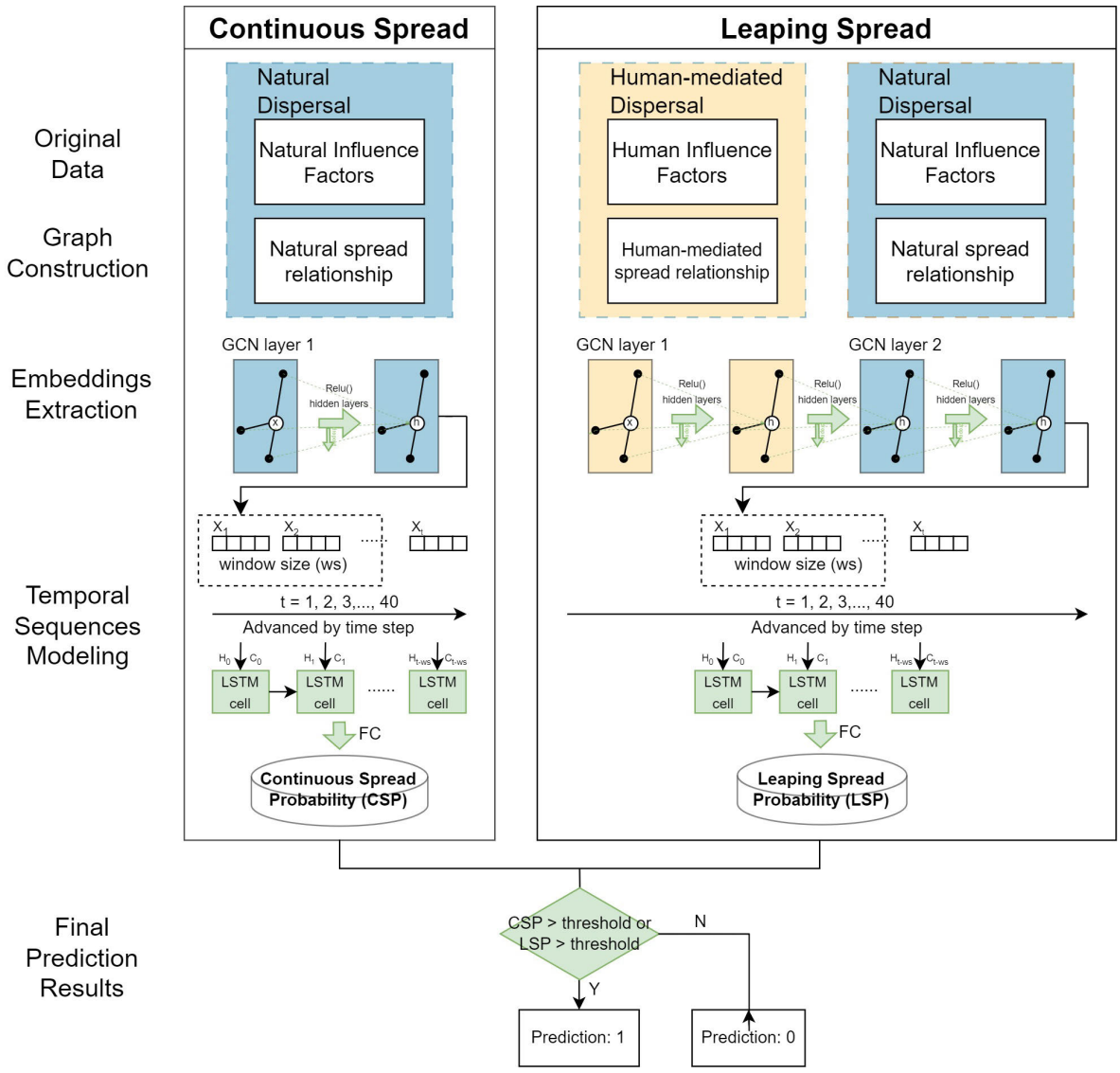


Fig. 3. Architecture of the proposed GCN-LSTM model in this study.

Given that PWD datasets are often characterized by a significant class imbalance, we employed a comprehensive suite of evaluation metrics. The selected indicators include accuracy, precision, recall, the $F1$-score, the ROC AUC, and Cohen's kappa coefficient [17], [46], [47]. The formulas are as follows:

$$\text{Accuracy} = \frac{\text{TP} + \text{TN}}{\text{P} + \text{N}} \tag{14}$$

$$\text{Precision} = \frac{\text{TP}}{\text{TP} + \text{FP}} \tag{15}$$

$$\text{Recall} = \frac{\text{TP}}{\text{TP} + \text{FN}} \tag{16}$$

$$F1\text{-score} = 2 \times \frac{\text{Precision} \times \text{Recall}}{\text{Precision} + \text{Recall}} \tag{17}$$

$$\text{Kappa} = \frac{P_o - P_e}{1 - P_e} \tag{18}$$

where P_o represents the observed accuracy, and P_e is the hypothetical probability of chance agreement.

IV. Results

A. Influencing Factors Analysis

1) Identification of Influencing Factors: From an initial set of 42 potential natural and human-mediated variables across China for the period 1982–2022, a two-stage screening process was implemented to identify the most robust factors of OPWD. The initial GeoDetector analysis revealed that all 42 candidate factors had a statistically significant influence ($p < 0.05$) on the spatial distribution of PWD [see Fig. 4(a)]. We first retained the top 50% of these variables based on their explanatory power (q-statistic). Subsequently, to mitigate multicollinearity, a Pearson correlation analysis was performed on this subset. For any pair of variables with a high correlation coefficient ($|R| > 0.7$), the one with the lower q-statistic was systematically excluded.

2) Interaction Between the Influencing Factors: We further employed the interaction detector to quantify the synergistic effects between the 16 selected drivers on OPWD. The analysis revealed that all pairwise combinations exhibited either

Authorized licensed use limited to: University of Chinese Academy of SciencesCAS. Downloaded on March 10,2026 at 08:18:33 UTC from IEEE Xplore. Restrictions apply.

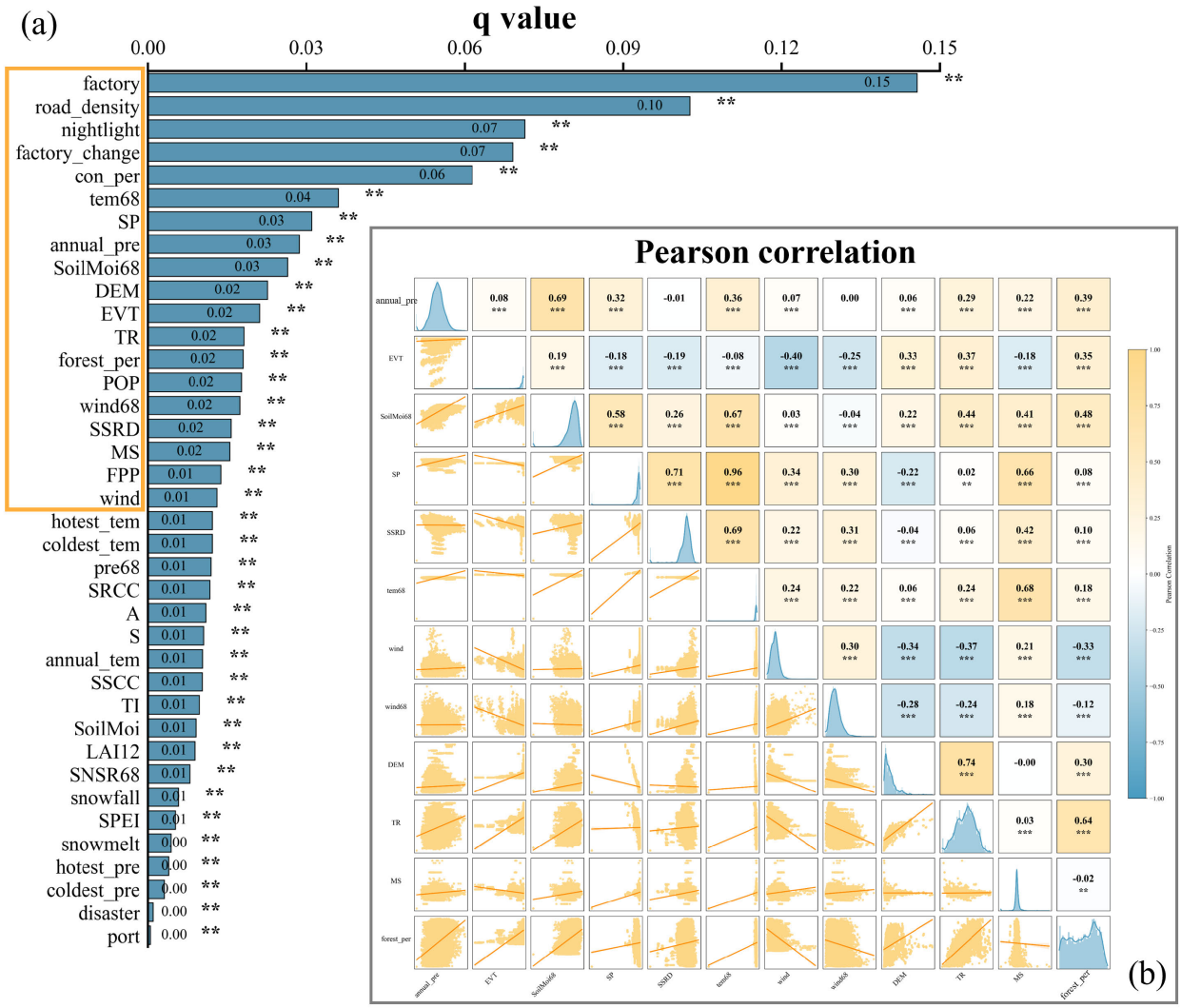


Fig. 4. Identification of potential influencing factors. (a) Result of factor detector analysis in GeoDetector and (b) Pearson correlation coefficient of nine natural factors.

bivariate or nonlinear enhancement, indicating that the combined explanatory power of any two factors was consistently greater than their individual effects (see Fig. 5). This underscores the presence of complex interdependent mechanisms of PWD spread, rather than isolated influences.

Notably, human-mediated factors were central to the strongest interactions. The five most powerful synergistic pairs all involved the factory variable, specifically its interaction with wind_{68} (q = 0.28), forest_per (q = 0.28), road_density (q = 0.24), con_per (q = 0.20), and nightlight (q = 0.20). The prevalence of nonlinear enhancement as the dominant interaction type confirms that the joint influence of these factors exceeded the maximum individual effect and occasionally simple additive expectations. This finding highlights the necessity of using nonlinear models or explicitly incorporating interaction terms to accurately capture the underlying pathogenic mechanisms and enhance the predictive power of PWD simulation systems.

3) Differentiation in the Contribution of Influencing Factors: Considering the extensive spatial and temporal scope of this study, we summarized the contribution of natural and human-mediated influencing factors to the OPWD, respectively, conducting GeoDetector analyses separately both temporally (by year) and spatially (by province) to quantify the contributions of factors to the OPWD, and then summarized these results in box plots (see Fig. 6).

Although human-mediated factors constituted a minority of the factors, they exhibited a higher contribution proportion (about 71%) with the greatest influence arising from factory, road_network, nightlight, factory_change, and con_per. In contrast, natural factors contributed more modestly and uniformly ($q \approx 0.10$) with tem_{68}, annual_pre, and SoilMoi_{68} being the most prominent, suggesting comparable levels of explanatory power, though not necessarily through identical causal pathways [48].

A comparison of the spatiotemporal analysis revealed significant differences in the stability of factors influencing. The contributions of the 16 factors remained relatively consistent over time, which suggests stable underlying processes on a national scale. However, their contributions exhibited marked

Authorized licensed use limited to: University of Chinese Academy of SciencesCAS. Downloaded on March 10,2026 at 08:18:33 UTC from IEEE Xplore. Restrictions apply.

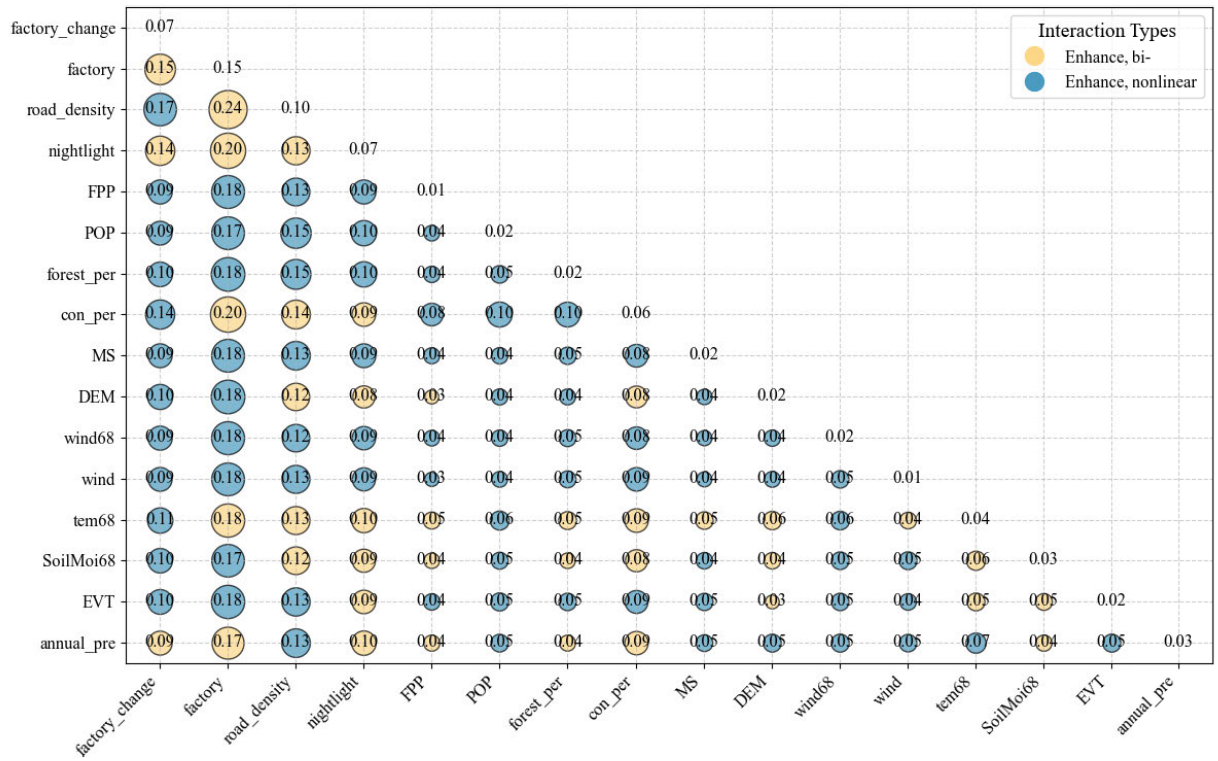


Fig. 5. Interactions between influencing factors explored by the interaction detector.

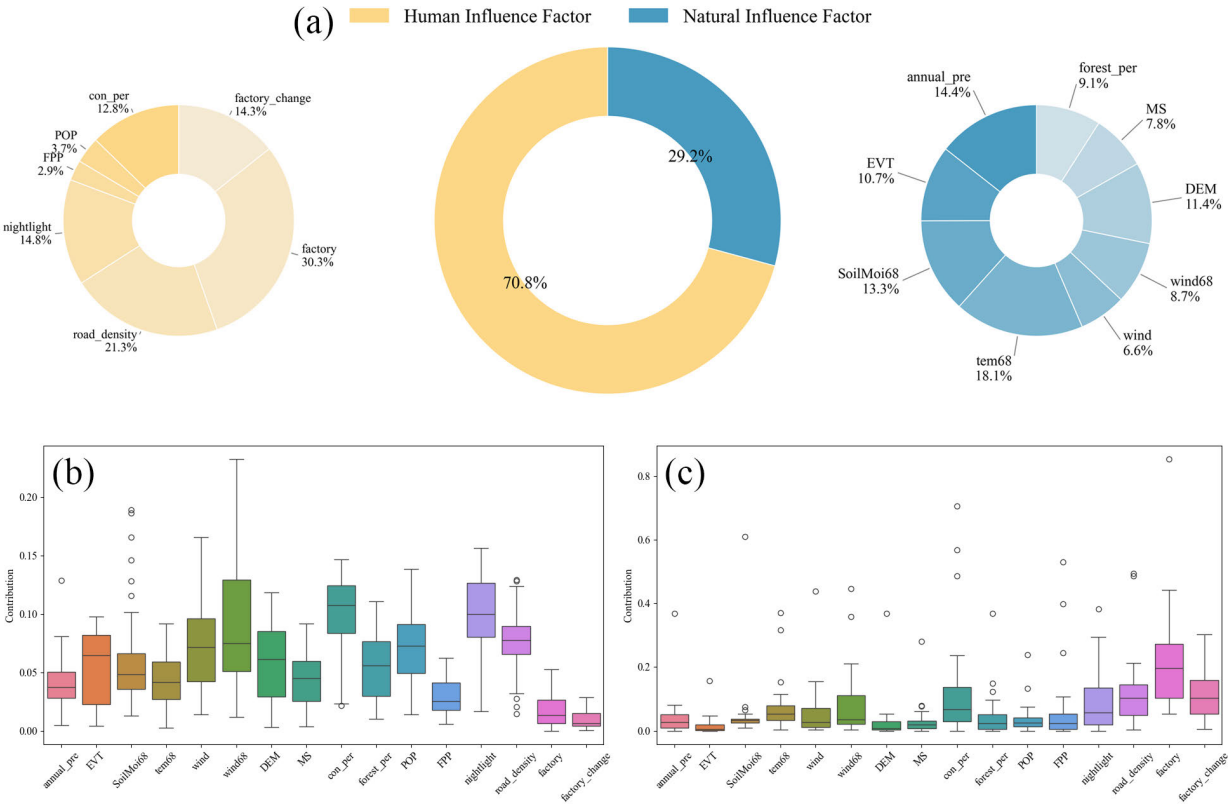


Fig. 6. Differentiation in the contribution of influencing factors. (a) Contribution of natural influencing factors and human-mediated factors to the OPWD, respectively. (b) Factor detector analysis in GeoDetector by year. (c) Factor detector analysis in GeoDetector by province.

spatial heterogeneity across provinces. Specific factors demonstrated high explanatory power only in localized regions, and conversely, the PWD dynamics in some provinces were strongly associated with only a limited subset of factors, which

Authorized licensed use limited to: University of Chinese Academy of SciencesCAS. Downloaded on March 10,2026 at 08:18:33 UTC from IEEE Xplore. Restrictions apply.

TABLE III
PERFORMANCE COMPARISON WITH BENCHMARK MODELS

Evaluation Index	GCN-LSTM	GCN	LSTM	MaxEnt	RF	XGBoost	SVM	CA-Markov	Compare
Accuracy	0.93	0.86	0.89	0.74	0.90	0.90	0.88	0.89	
Precision	0.81	0.69	0.72	0.36	0.83	0.77	0.71	0.97	
Recall	0.79	0.24	0.69	0.66	0.54	0.60	0.47	0.37	
F1 Score	0.80	0.36	0.71	0.46	0.65	0.68	0.56	0.54	
ROC AUC	0.87	0.72	0.82	0.71	0.76	0.78	0.71	0.69	
Kappa	0.75	0.30	0.64	0.31	0.60	0.62	0.50	0.49	

highlights the critical need for a spatially explicit modeling approach that can adapt to local variations.

B. Model Prediction Results

1) Accuracy Validation of OPWD: In our study, the data from the first five years were used to predict the next year's OPWD, and a rolling prediction was conducted year by year. The validation result is highly accurate, with an accuracy of 0.93, a precision of 0.81, a recall of 0.79, a $F1$ of 0.80, a ROC AUC of 0.87, and a kappa of 0.75 between the predicted value and the actual value, signifying substantial agreement between predictions and ground-truth observations. This robust performance was achieved using the optimal hyperparameter configuration identified during the tuning process (hidden_dims = 128, learning_rate = 0.001, dropout = 0.4, weight_decay = 1e-04, and thresholds = 0.45).

For clarity of presentation, Fig. 7 illustrates the model's predictions at representative five-year intervals. The complete year-by-year spatiotemporal simulation results are provided in Supplementary Fig. 1. The maps illustrate a clear and progressive expansion of the disease from its initial epicenters in the Yangtze River Delta. In the early years, high CSP is concentrated within and adjacent to existing PWD-affected counties. Over time, the model captures both the infilling of existing disease clusters and, critically, the emergence of new, distant infection foci characterized by high LSP. This pattern becomes particularly pronounced lately, showing extensive new potential outbreaks far from established disease fronts, reflecting the increasing role of leaping spread.

The model's ability to explicitly disentangle these two transmission pathways provides critical insight into the disease's invasion mechanism. High CSP values effectively delineate the frontiers of established outbreaks, where management should focus on containment and local eradication. In contrast, high LSP values function as an early warning system, identifying counties at high risk of new introductions, likely driven by the human-mediated factors identified in our earlier analysis. This framework thus offers a more nuanced and actionable understanding of PWD risk that can directly inform differentiated prevention and control strategies.

2) Comparison With Other Models: To benchmark the GCN-LSTM model, its performance was compared against five established methods commonly used in disease risk modeling: maximum entropy (MaxEnt), RF, XGBoost, support vector machine (SVM), and a CA–Markov model [8], [14], [17], [18], [24], [26], [49], [50], [51], [52], [53]. Furthermore, to provide a deeper validation against contemporary deep learning baselines, we also included comparisons with a pure GCN and a pure LSTM model. As presented in Table III, the GCN-LSTM model surpassed all benchmark models in overall performance, particularly in achieving a balance between competing metrics. While models like RF and CA–Markov achieved high precision, this came at the cost of critically low recall, indicating a strong bias toward predicting a strong bias toward predicting the major negative class and a failure to identify a large proportion of actual PWD cases. In the context of disease prediction, high recall is paramount to minimize the risk of overlooking infected areas. The MaxEnt model showed the opposite bias, overpredicting PWD presence, which resulted in poor precision. Although XGBoost demonstrated a better balance, its overall metrics remained inferior to our proposed model. The pure GCN model struggled with the long-term temporal forecasting task, while the pure LSTM model was limited by its inability to leverage explicit spatial dependencies. This result underscores the necessity and effectiveness of our integrated architecture that simultaneously captures spatial and temporal dynamics. Notably, the GCN-LSTM model excelled without

Authorized licensed use limited to: University of Chinese Academy of SciencesCAS. Downloaded on March 10,2026 at 08:18:33 UTC from IEEE Xplore. Restrictions apply.

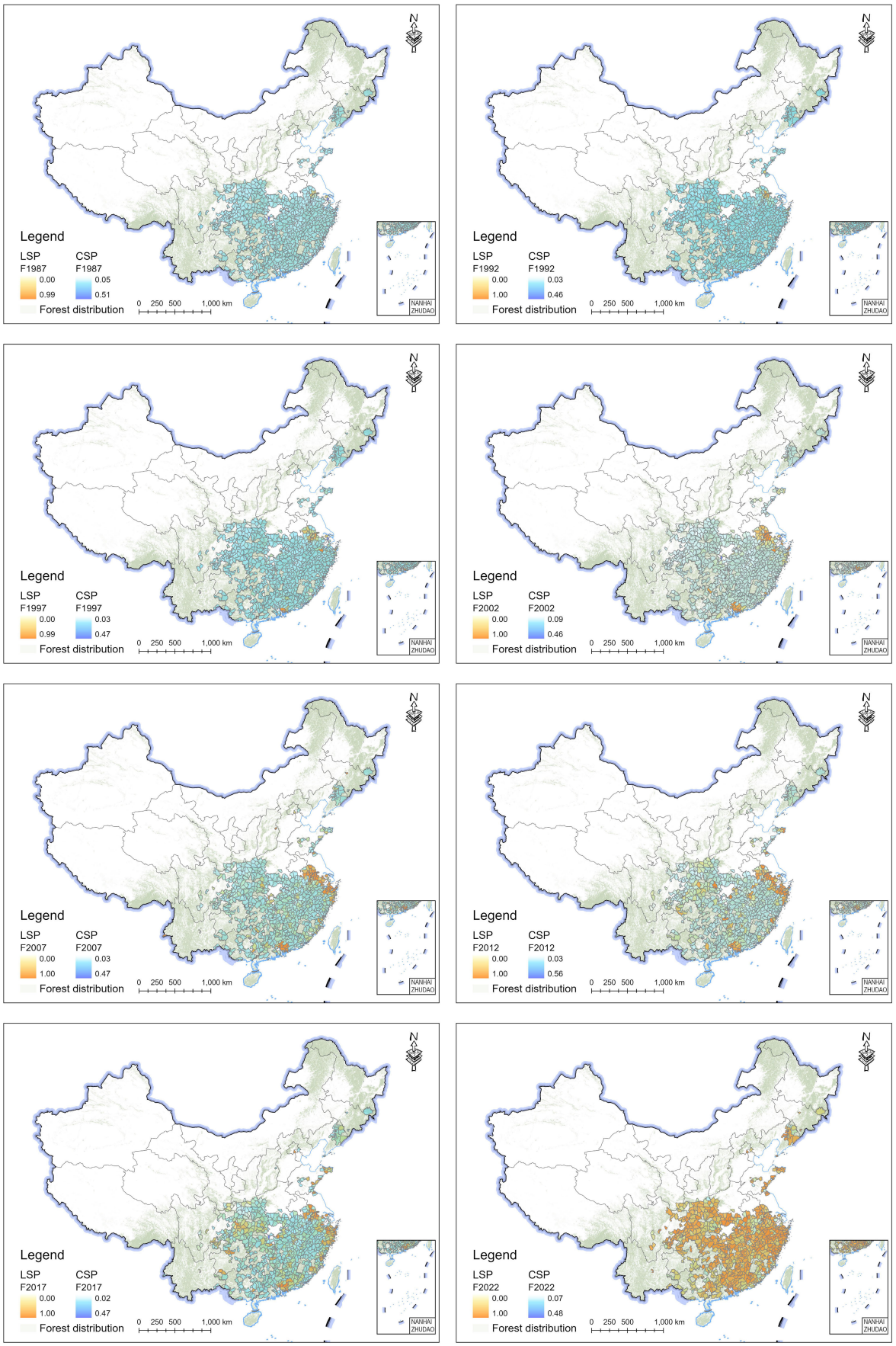


Fig. 7. LSP and CSP predicted by GCN-LSTM from the period 1987–2022 every five years.

Authorized licensed use limited to: University of Chinese Academy of SciencesCAS. Downloaded on March 10,2026 at 08:18:33 UTC from IEEE Xplore. Restrictions apply.

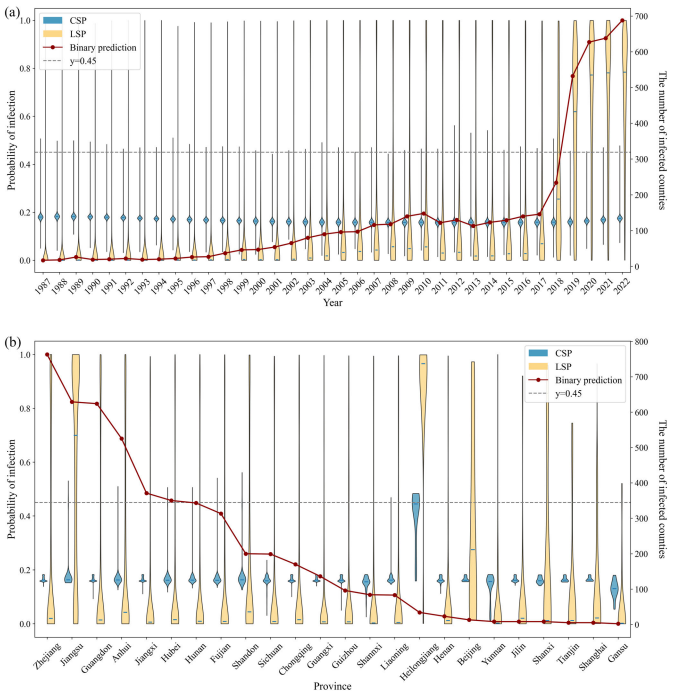


Fig. 8. Model-predicted spatiotemporal dynamics of OPWD. (a) Interannual variations in transmission probabilities alongside cumulative epidemic counties. (b) Provincial-level spread probabilities correlated with outbreak frequency alongside affected counties in each province (ranked from most to least).

requiring manual class weight adjustments (e.g., assigning higher penalty weights to minority classes during training), demonstrating an intrinsic capability to handle class imbalance and providing more reliable and balanced predictions for operational vegetation health monitoring.

3) Spatial and Temporal Trends of OPWD: The historical record of PWD outbreaks in China for the period 1982–2022 reveals a complex spatiotemporal evolution [see Fig. 8(a)]. To investigate the underlying mechanisms, this study developed a GCN-LSTM model to deconstruct the PWD propagation into its distinct transmission modes. The spatiotemporal evolution trend of the model prediction results is shown in Fig. 8.

From a temporal perspective, the statistical CSP exhibited minimal fluctuations between 1987 and 2022, maintaining a stable mean around 17% in the majority. In contrast, LSP initially approximated zero during early epidemic stages, followed by a gradual increase, an intermediate plateau with slight decline, and a recent sharp escalation, which is paralleled by the temporal pattern of cumulative PWD-affected counties nationwide. These temporal dynamics align with empirical observations and corroborate findings from Hao Zhuoqing et al.'s research [26]. Spatially, CSP demonstrated limited provincial variability except in Heilongjiang Province (elevated) and Gansu Province (depressed). Conversely, LSP exhibited pronounced spatial heterogeneity across provinces. High CSP zones are concentrated in Heilongjiang, Shandong, Fujian, Jiangsu, Anhui, Hubei, and Hunan provinces, while LSP hotspots emerged in Heilongjiang, Jiangsu, Beijing, Shanxi, Anhui, and Shandong. Among the five most frequently affected provinces, Zhejiang, Guangdong, and Jiangxi predominantly experienced leaping spread, Jiangsu and Anhui exhibited dual transmission mechanisms with both continuous and leaping patterns, while Guangdong showed higher LSP than Jiangxi. Notably, Heilongjiang Province manifested elevated risks for both transmission modes, necessitating prioritized prevention and control measures. This analysis reveals distinct spatiotemporal differentiation patterns: leaping spread demonstrates significant variability across both temporal and spatial dimensions, whereas continuous spread primarily differentiates spatially.

4) Response Relationship of Influencing Factors to the OPWD: To systematically elucidate the impact of influencing factors on the two transmission modes of PWD and to improve the interpretability of the GCN-LSTM model, we conducted a feature importance analysis based on model outputs, which is visualized through detailed response plots. These plots illustrate the relationship between the CSP and nine natural factors for continuous spread, and between LSP and 16 influencing factors for leaping spread (see Fig. 9). This analytical approach demonstrates how each influencing factor affects the predicted probability (CSP or LSP) at different values, thereby providing direct insight into the model's internal reasoning and the relative contribution of different drivers. The analysis reveals a distinct dichotomy: the CSP is predominantly governed by natural environmental factors that collectively define the pathogen's fundamental ecological niche, whereas LSP is overwhelmingly driven by human-mediated factors that facilitate long-distance cross-regional spread.

The CSP exhibits complex, nonlinear responses to natural environmental variables, indicating the existence of specific ecological thresholds for its occurrence [see Fig. 9(a)]. Topography acts as a primary constraint, with CSP being most concentrated at low-to-mid elevations (DEM $\approx$ 0–700 m) and diminishing significantly at higher altitudes. This suggests that high-altitude environments are less conducive to the sustained local spread of PWD. Similarly, hydrothermal conditions define an optimal habitat window. The response to average summertime temperature (tem_{68}) is distinctly unimodal, peaking near 300 K ($\approx$ 27 °C), while the response to annual precipitation ($annual_pre$) also displays a unimodal trend, implying that both extremely dry and excessively moist conditions inhibit continuous spread. Furthermore, moderate summer and annual wind speeds ($wind_{68}$, $wind$) and a specific range of MS index (MS $\approx$ 60) are associated with elevated CSP. Notably, the highest CSP occurs in areas with lower forest area percentage ($forest_per$), suggesting that fragmented landscapes or forest edges may facilitate localized spread. Collectively, these response patterns delineate the biophysical envelope for the continuous spread of PWD, providing critical parameters for ecological risk assessment.

In stark contrast, the LSP is predominantly governed by human-mediated factors [see Fig. 9(b)]. The LSP increases markedly in areas with developed transportation networks, as evidenced by the sharp rise in high-probability events once road network density ($road_density$) surpasses a low baseline level. Socio-economic indicators also show strong positive relationships with LSP. For instance, nighttime-light intensity ($nightlight$), wood-processing factory density ($factory$), and the change in factory numbers ($factory_change$) all demonstrate

Authorized licensed use limited to: University of Chinese Academy of SciencesCAS. Downloaded on March 10,2026 at 08:18:33 UTC from IEEE Xplore. Restrictions apply.

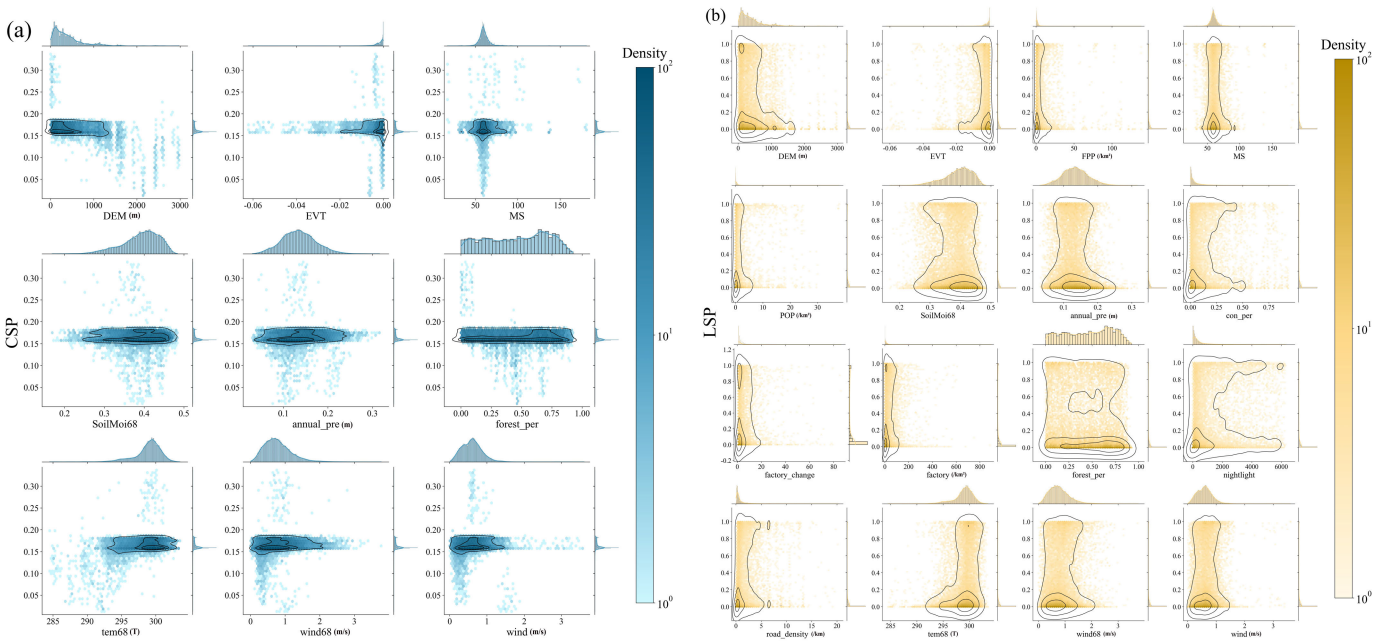


Fig. 9. Response relationship of influencing factors to (left) CSP and (right) LSP. (a) Response relationship of natural influencing factors to the continuous spread probability (CSP). (b) Response relationship of natural and human-mediated influencing factors to the leaping spread probability (LSP).

that areas with higher intensity human activity correspond to a greater frequency and magnitude of high-probability LSP events. This pattern is not a simple linear increase but rather an expansion of risk potential at higher indicator values. Furthermore, the analysis of forest proximate population (FPP) and population mobility (POP) reveals a nuanced relationship: peak risk occurs not in the most densely populated urban cores, but in moderately developed peri-urban or rural areas where human activity extensively interfaces with susceptible forest landscapes. This highlights the critical role of the forest-urban interface in facilitating long-range PWD jumps.

While human activities are the primary drivers of leaping spread, these events still occur within a "permissive natural envelope" defined by the same environmental factors that constrain continuous spread. For instance, both CSP and LSP peak at low elevations (DEM), moderate temperatures (tem_{68}), and a MS index around 60. However, there's a little bit different for forest area percentage ($forest_per$): while CSP thrives in low-coverage areas, LSP is highest in regions with moderate-to-high forest cover. This suggests that continuous spread is a phenomenon of the forest edge, whereas leaping spread, intrinsically linked to the transport of infected timber and wood products, is naturally more prevalent in regions with substantial forest resources available for logging and processing. These findings unequivocally demonstrate that managing human-mediated pathways is paramount for preventing the rapid, large-scale expansion of PWD.

V. Discussion

Our study successfully developed and validated a GCN-LSTM model to deconstruct the complex spatiotemporal dynamics of PWD in China, differentiating between local continuous spread and long-distance leaping spread. The following discussion interprets these findings in the context of existing literature, highlights the methodological advantages of our approach, and outlines key limitations and future research directions.

A. Influencing Factors Response to OPWD

The dichotomy between natural and human-mediated factors provides a fundamental basis for predictive modeling, as it directly structures and informs the GCN-LSTM framework. This distinction enables the explicit representation of two dominant transmission mechanisms: continuous spread and leaping spread. Continuous spread, governed by stable natural factors (e.g., temperature, precipitation, elevation), defines a relatively constant ecological niche, aligning with the known ecophysiological constraints of the nematode and its vector [14], [17]. The model's CSP output captures this stability through predictable, often nonlinear responses to these factors (see Fig. 9), thereby identifying areas of persistent, endemic risk suitable for long-term management. In contrast, leaping spread is driven by dynamic anthropogenic factors such as wood-processing factory density and road network density. The model's LSP is critical for early warning systems, enabling timely interception of transport pathways and regulation of high-risk activities.

Crucially, these two types of processes and factors do not operate independently. GeoDetector analysis revealed significant nonlinear and bivariate enhancement interactions, particularly among anthropogenic drivers (e.g., factory density with road density). This statistical evidence is meaningfully captured and operationalized within the GCN-LSTM framework. First, synergistic interactions are structurally embedded in the graph architecture: the human-mediated spread network explicitly links high factory-density counties (sources) to high timber-demand areas via the road network, thereby hard-coding the synergy identified by GeoDetector. Second,

Authorized licensed use limited to: University of Chinese Academy of SciencesCAS. Downloaded on March 10,2026 at 08:18:33 UTC from IEEE Xplore. Restrictions apply.

graph convolution operations naturally simulate the spatial consequences of these interactions by aggregating and amplifying risk signals across connected nodes, translating static bivariate enhancement into a dynamic spatial diffusion process. Finally, while GeoDetector quantifies interaction strength, the GCN-LSTM translates this understanding into actionable spatial predictions. The model's learned representations implicitly encode these relationships, with the resulting CSP and LSP outputs and response curves (see Fig. 9) demonstrating that the highest probabilities occur where synergistic driver pairs co-locate. This provides an intuitive, managerially relevant visualization of how factor interactions translate into concrete outbreak risk.

B. Spatiotemporal Differentiation of PWD Spread Mechanisms

By deconstructing PWD spread into two distinct mechanisms, our model provides novel insights into the epidemic's spatiotemporal behavior. Continuous spread acts as a stable endemic pressure that facilitates localized intensification within suitable habitats. Its probability remained relatively constant over time, suggesting a persistent background risk. In contrast, the leaping spread is the primary engine of the disease's large-scale, epidemic expansion. Its temporal trend, marked by a recent sharp escalation, directly parallels the cumulative increase in affected counties.

Our finding that in severely affected areas, provinces like Jiangsu and Anhui are dominated by leaping spread, while others like Zhejiang and Guangdong exhibit continuous spread, highlights the need for spatially tailored management strategies. Based on our model predictions, we propose specific threshold-based intervention strategies to guide resource allocation. For regions with a high CSP, management should prioritize local containment measures, such as sanitation logging, vector beetle control, and the establishment of protective buffer zones around infected areas. Conversely, in areas with a high LSP, the focus must shift to interception and quarantine strategies, which include enhanced surveillance at key transportation hubs and wood-processing facilities, alongside strict regulation of wood product movement. Notably, regions exhibiting both high CSP and LSP represent dual high-risk zones that demand integrated management, combining the aforementioned approaches with maximum resource allocation to establish them as the top priority for comprehensive prevention and control efforts. These threshold-based recommendations provide forest managers with actionable criteria for optimizing limited resources while effectively addressing both transmission pathways.

C. Advantages of GCN-LSTM

In this study, we propose a novel GCN-LSTM algorithm, which differs significantly from the conventional approaches in most improved deep learning algorithms. Most improved deep learning algorithms focus on enhancing a single existing algorithm by modifying its structure, activation function, and other elements to build faster and more accurate models [54], [55]. In contrast, our approach aims to address application challenges by developing a deep learning algorithm that can be applied in China accurately and extract complex spatiotemporal features, especially in regions with high spatial heterogeneity.

The superior performance of the GCN-LSTM model over established benchmarks stems from its intrinsic ability to capture the complex spatiotemporal dependencies inherent in disease propagation. Unlike traditional models that treat spatial units as independent, the GCN component integrates information from both adjacent and distant-but-connected high-risk areas, which is essential for modeling leaping events driven by transportation and trade networks [56], [57]. Simultaneously, the LSTM component effectively captures temporal autocorrelation, the capacity of which to "remember" past states is critical for predicting the evolution of a multiyear epidemic. The GCN-LSTM algorithm, therefore, integrates the strengths of various deep learning models, utilizing them to extract diverse features from remote sensing data to achieve high-accuracy PWD prediction. The model's exceptional balance between precision (0.81) and recall (0.79), achieved without manual class re-weighting, is particularly noteworthy. In disease monitoring and warning where failing to detect an outbreak (low recall) has severe consequences, this balanced performance makes the GCN-LSTM a reliable and operationally valuable tool for public health and forest management authorities compared to models that may be biased toward predicting nonoccurrence [58], [59].

D. Limitations and Prospects

In this study, an innovative framework for PWD prediction is proposed by integrating prior knowledge with a GCN-LSTM model. However, there are still some limitations that cannot be ignored.

1) The current lack of detailed data for certain human-mediated factors (e.g., finer-scale timber product flow data) and some large-scale biological data (e.g., vector abundance, host-tree health/species composition) may introduce uncertainty into the study.
2) Although the framework performed well in China, its effectiveness in other countries facing PWD threats (e.g., Japan, South K, or European nations) with different ecological and socioeconomic conditions remains unvalidated.
3) The model development and validation primarily focused on a large scale. The verification of fine-grained, small-scale results requires further advancement and refinement.
4) The training process of the proposed deep learning framework is computationally intensive, which could be a limiting factor for operational implementation in some resource-constrained environments.

Future research should therefore prioritize three key directions to address these limitations and advance predictive capability as follows.

1) Future work should prioritize acquiring and integrating multisource, high-resolution spatiotemporal data, including more direct metrics of human activity and remote

Authorized licensed use limited to: University of Chinese Academy of SciencesCAS. Downloaded on March 10,2026 at 08:18:33 UTC from IEEE Xplore. Restrictions apply.

sensing data for early detection of biotic stress, to optimize model inputs.

2) Exploring transfer learning techniques is crucial for efficiently adapting the model to new geographical and outbreak contexts [60], [61]. This involves reconstructing graph structures based on local dynamics and recalibrating key parameters, such as forest composition, human activity networks, and climate.
3) The next step involves conducting targeted small-scale regional validations in diverse environments by integrating high-resolution environmental and socio-economic data for county or forest-farm level case studies. This will further test the model's transferability, provide concrete examples of its predictive mechanisms, and bridge the gap between macroscale forecasting and local-scale management.
4) Future work can focus on optimizing the model architecture to balance predictive performance with computational efficiency, thereby enhancing its practicality for broader operational deployment.

VI. Conclusion

This study introduces a novel, mechanism-coupled framework that integrates prior knowledge with a customized GCN-LSTM model to deconstruct and predict the spatiotemporal dynamics of PWD in China from the period 1982 to 2022. The model demonstrated superior predictive performance over established benchmarks (accuracy = 0.93 and ROC AUC = 0.87), a success attributed to its capacity to capture the complex non-Euclidean spatial dependencies and long-term temporal autocorrelation inherent in PWD spread through a specifically designed dichotomy mechanism. While natural factors primarily define the fundamental ecological niche, leading to stable and localized continuous spread, human-mediated factors are the architects of its rapid, long-distance leaping spread. This mechanistic deconstruction not only explains the observed historical patterns of PWD spread but also underscores the necessity of a dual-pronged management strategy that addresses both ecological susceptibility and human-mediated pathways.

The theoretical contribution of this research lies in advancing the application of geospatial AI through a complete research paradigm. This paradigm is characterized by: 1) a comprehensive, ecologically and sociologically meaningful indicator system built upon 42 meticulously screened influencing factors; 2) a unique, mechanism-coupled dual-graph GCN-LSTM framework that explicitly models and distinguishes continuous and leaping PWD transmission pathways based on their underlying ecological and human-mediated mechanisms; and 3) an innovative integration of the interpretable GeoDetector with the deep learning model, enabling a deep fusion of data-driven prediction with domain-knowledge interpretation. This ensures our findings provide both high predictive accuracy and profound mechanistic insights into the complex, interacting factors of biological invasions.

Beyond its theoretical advancements, this work offers substantial practical value. The highly accurate tool for long-term PWD forecasting and warning, along with the high-resolution risk maps generated, provides critical, spatially explicit guidance for forestry agencies. This enables the formulation of targeted, resource-efficient policies to enhance sustainable forest management and biosecurity and offers a robust analytical paradigm and a valuable scientific basis for confronting the escalating threat of PWD and other invasive species in an increasingly interconnected world.

References

[1] M. A. Back, L. Bonifácio, M. L. Inácio, M. Mota, and E. Boa, "Pine wilt disease: A global threat to forestry," *Plant Pathol.*, vol. 73, no. 5, pp. 1026–1041, Jun. 2024.

[2] Y. Mamiya, "Pathology of the pine wilt disease caused by bursaphelenchus xylophilus," *Annu. Rev. Phytopathol.*, vol. 21, no. 1, pp. 201–220, Sep. 1983.

[3] X. Tang, Y. Yuan, X. Li, and J. Zhang, "Maximum entropy modeling to predict the impact of climate change on pine wilt disease in China," *Frontiers Plant Sci.*, vol. 12, Apr. 2021, Art. no. 652500.

[4] H. R. Cheng, M. S. Lin, W. Q. Li, and Z. D. Fang, "The occurrence of a pine wilting disease caused by a nematode found in Nanjing," *Forest Pest Disease*, vol. 1983, no. 4, pp. 1–5, 1983.

[5] B. Zhao, K. Futai, J. Sutherland, and Y. Takeuchi, *Pine Wilt Disease*. Tokyo, Japan: Springer, 2008.

[6] W. Wang, W. Peng, X. Liu, G. He, and Y. Cai, "Spatiotemporal dynamics and factors driving the distributions of pine wilt disease-damaged forests in China," *Forests*, vol. 13, no. 2, p. 261, Feb. 2022.

[7] X.-Z. Wang, X. Wang, S.-F. Zhang, Y.-L. Zhang, Y.-F. Cao, and L.-F. Wang, "The effect of pine wood nematode bursaphelenchus xylophilus (Steiner and Buhrer) nickle on intestinal bacterial community of insect vector monochamus saltuarius (Coleoptera: Cerambycidae)," *Forests*, vol. 13, no. 10, p. 1673, Oct. 2022.

[8] R. Gao, L. Liu, R. Li, S. Fan, J. Dong, and L. Zhao, "Predicting potential distributions of monochamus saltuarius, a novel insect vector of pine wilt disease in China," *Frontiers Forests Global Change*, vol. 6, Sep. 2023, Art. no. 1243996, doi: 10.3389/ffgc.2023.1243996.

[9] E. G. Brockerhoff et al., "Forest biodiversity, ecosystem functioning and the provision of ecosystem services," *Biodiversity Conservation*, vol. 26, no. 13, pp. 3005–3035, Dec. 2017.

[10] J. Zhao, J. Huang, J. Yan, and G. Fang, "Economic loss of pine wood nematode disease in Mainland China from 1998 to 2017," *Forests*, vol. 11, no. 10, p. 1042, Sep. 2020.

[11] C. Robinet, N. Van Opstal, R. Baker, and A. Roques, "Applying a spread model to identify the entry points from which the pine wood nematode, the vector of pine wilt disease, would spread most rapidly across Europe," *Biol. Invasions*, vol. 13, no. 12, pp. 2981–2995, Dec. 2011.

[12] N. Shigesada, K. Kawasaki, and Y. Takeda, "Modeling stratified diffusion in biological invasions," *Amer. Naturalist*, vol. 146, no. 2, pp. 229–251, Aug. 1995.

[13] K. Togashi and N. Shigesada, "Spread of the pinewood nematode vectored by the Japanese pine sawyer: Modeling and analytical approaches," *Population Ecology*, vol. 48, no. 4, pp. 271–283, Oct. 2006.

[14] X. Ouyang, A. Chen, Y. Li, X. Han, and H. Lin, "Predicting the potential distribution of pine wilt disease in China under climate change," *Insects*, vol. 13, no. 12, p. 1147, Dec. 2022.

[15] F. Wang, "Pine wilt in meteorological hazard environments," *Natural Hazards*, vol. 72, no. 2, pp. 723–741, Jun. 2014.

[16] W. Wang, Q. Zhu, G. He, X. Liu, W. Peng, and Y. Cai, "Impacts of climate change on pine wilt disease outbreaks and associated carbon stock losses," *Agricult. Forest Meteorol.*, vol. 334, May 2023, Art. no. 109426.

[17] Z. Hao, G. Fang, W. Huang, H. Ye, B. Zhang, and X. Li, "Risk prediction and variable analysis of pine wilt disease by a maximum entropy model," *Forests*, vol. 13, no. 2, p. 342, Feb. 2022.

[18] D. Liu and X. Zhang, "Occurrence prediction of pine wilt disease based on CA–Markov model," *Forests*, vol. 13, no. 10, p. 1736, Oct. 2022.

[19] A. M. Liebhold and P. C. Tobin, "Population ecology of insect invasions and their management," *Annu. Rev. Entomology*, vol. 53, no. 1, pp. 387–408, Jan. 2008.

[20] J. D. Murray, *Mathematical Biology: I. An Introduction*, vol. 17, 3rd ed., Cham, Switzerland: Springer, 2007.

[21] N. Shigesada and K. Kawasaki, *Biological Invasions: Theory and Practice*, 1st ed., Oxford, U.K.: Oxford University Press, 1997.

Authorized licensed use limited to: University of Chinese Academy of SciencesCAS. Downloaded on March 10,2026 at 08:18:33 UTC from IEEE Xplore. Restrictions apply.

[22] T. Pukkala, T. Möykkynen, and C. Robinet, "Comparison of the potential spread of pinewood nematode (Bursaphelenchus xylophilus) in Finland and Iberia simulated with a cellular automaton model," *Forest Pathol.*, vol. 44, no. 5, pp. 341–352, 2014.

[23] Z. Hao, J. Huang, Y. Zhou, and G. Fang, "Spatiotemporal pattern of pine wilt disease in the Yangtze river basin," *Forests*, vol. 12, no. 6, p. 731, Jun. 2021.

[24] N. Aierken et al., "Assessing global pine wilt disease risk based on ensemble species distribution models," *Ecol. Indicators*, vol. 167, Oct. 2024, Art. no. 112691.

[25] H. Zhao et al., "Risk assessment framework for pine wilt disease: Estimating the introduction pathways and multispecies interactions among the pine wood nematode, its insect vectors, and hosts in China," *Sci. Total Environ.*, vol. 905, Dec. 2023, Art. no. 167075.

[26] Z. Hao et al., "Long-term spatiotemporal pattern and temporal dynamic simulation of pine wilt disease," *Remote Sens.*, vol. 17, no. 3, p. 348, Jan. 2025.

[27] M. F. Guerri, C. Distante, P. Spagnolo, F. Bougourzi, and A. Taleb-Ahmed, "Deep learning techniques for hyperspectral image analysis in agriculture: A review," *ISPRS Open J. Photogramm. Remote Sens.*, vol. 12, Apr. 2024, Art. no. 100062.

[28] W. Wu et al., "Research progress on the early monitoring of pine wilt disease using hyperspectral techniques," *Sensors*, vol. 20, no. 13, p. 3729, Jul. 2020.

[29] E. M. H. I. Ekanayaka and P. P. N. V. Kumara, "Machine learning approach for new crop disease predict and alert system: A review," in *Proc. Int. Conf. Emerg. Techn. Comput. Intell. (ICETCI)*, Aug. 2022, pp. 45–49.

[30] Z. Kai, J. Liang, D. Yan, and X. Zhang, "Research advances of pine wood nematode disease in China," *World Forestry Research*, vol. 3, no. 23, pp. 59–63, 2010.

[31] J. Shengwei, W. Hao, L. Debin, L. Zaiquan, H. Shan, and S. Yushuang, "Analysis on disaster characteristics of pine wood nematode in Northeast China," *Zhongguo Senlin Bing Chong*, vol. 41, no. 4, pp. 9–15, 2022.

[32] Y. Jianren and W. Xiaoqin, "Research progress on pine wood nematode disease," *Forest Diseases Insects China*, vol. 2022, no. 3, pp. 1–10, 2022.

[33] L. Zhang, Z. Ren, B. Chen, P. Gong, B. Xu, and H. Fu, "A prolonged artificial nighttime-light dataset of China (1984–2020)," *Sci. Data*, vol. 11, no. 1, p. 414, Apr. 2024.

[34] A. Carioli, M. Schiavina, K. J. MacManus, and S. Freire, "GHS-POP R2023A–GHS population grid multitemporal (1975–2030)," Eur. Commission, Joint Res. Centre (JRC), Brussels, Belgium, 2023, doi: 10.2905/2FF68A52-5B5B-4A22-8F40-C41DA8332CFE.

[35] J.-F. Wang et al., "Geographical detectors-based health risk assessment and its application in the neural tube defects study of the heshun region, China," *Int. J. Geographical Inf. Sci.*, vol. 24, no. 1, pp. 107–127, Jan. 2010.

[36] W. Li et al., "Nonlinear effects of surface soil moisture changes on vegetation greenness over the Tibetan Plateau," *Remote Sens. Environ.*, vol. 302, Mar. 2024, Art. no. 113971.

[37] J. Yan et al., "New 30-m resolution dataset reveals declining soil erosion with regional increases across Chinese Mainland (1990–2022)," *Remote Sens. Environ.*, vol. 323, Jun. 2025, Art. no. 114681.

[38] J.-F. Wang and Y. Hu, "Environmental health risk detection with GeogDetector," *Environ. Model. Softw.*, vol. 33, pp. 114–115, Jul. 2012.

[39] D. Hu, Q. Meng, L. Zhang, and Y. Zhang, "Spatial quantitative analysis of the potential driving factors of Land Surface Temperature in different," *Sci. Total Environ.*, vol. 706, p. 135244, Jul. 2020.

[40] J. Wang and C. Xu, "Geodetector: Principle and prospective," *Acta Geographica Sinica*, vol. 72, no. 1, pp. 116–134, 2017.

[41] A. Hirata et al., "Potential distribution of pine wilt disease under future climate change scenarios," *PLoS ONE*, vol. 12, no. 8, Aug. 2017, Art. no. e0182837.

[42] F. R. Chung, *Spectral Graph Theory*, vol. 92. Providence, RI, USA: American Mathematical Soc., 1997.

[43] Y. Qi, Q. Li, H. Karimian, and D. Liu, "A hybrid model for spatiotemporal forecasting of $PM_{2.5}$ based on graph convolutional neural network and long short-term memory," *Sci. Total Environ.*, vol. 664, pp. 1–10, May 2019.

[44] Y. Zhang, P. Liu, and F. Biljecki, "Knowledge and topology: A two layer spatially dependent graph neural networks to identify urban functions with time-series street view image," *ISPRS J. Photogramm. Remote Sens.*, vol. 198, pp. 153–168, Apr. 2023.

[45] S. Hochreiter and J. Schmidhuber, "Long short-term memory," *Neural Comput.*, vol. 9, no. 8, pp. 1735–1780, Nov. 1997.

[46] N. M. DeLuca, B. F. Zaitchik, S. D. Guikema, J. M. Jacobs, B. J. K. Davis, and F. C. Curriero, "Evaluation of remotely sensed prediction and forecast models for vibrio parahaemolyticus in the Chesapeake bay," *Remote Sens. Environ.*, vol. 250, Dec. 2020, Art. no. 112016.

[47] J. M. Lobo, A. Jiménez-Valverde, and R. Real, "AUC: A misleading measure of the performance of predictive distribution models," *Global Ecol. Biogeography*, vol. 17, no. 2, pp. 145–151, Mar. 2008.

[48] J. Gu et al., "A method for hand-foot-mouth disease prediction using GeoDetector and LSTM model in Guangxi, China," *Sci. Rep.*, vol. 9, no. 1, p. 17928, Nov. 2019.

[49] L. Chen et al., "Modeling the distribution of pine wilt disease in China using the ensemble models MaxEnt and CLIMEX," *Ecology Evol.*, vol. 14, no. 9, p. 70277, Sep. 2024.

[50] M. Ikegami and T. A. R. Jenkins, "Estimate global risks of a forest disease under current and future climates using species distribution model and simple thermal model–pine wilt disease as a model case," *Forest Ecol. Manage.*, vol. 409, pp. 343–352, Feb. 2018.

[51] D.-S. Lee, W. I. Choi, Y. Nam, and Y.-S. Park, "Predicting potential occurrence of pine wilt disease based on environmental factors in South Korea using machine learning algorithms," *Ecol. Informat.*, vol. 64, Sep. 2021, Art. no. 101378.

[52] S. Sarkar, V. Sagan, S. Bhadra, K. Rhodes, M. Pokharel, and F. B. Fritschi, "Soybean seed composition prediction from standing crops using PlanetScope satellite imagery and machine learning," *ISPRS J. Photogramm. Remote Sens.*, vol. 204, pp. 257–274, Oct. 2023.

[53] L. I. U. Tingting, Y. Jinfan, Z. Ruliang, and L. I. U. Lin, "Prediction of spread risk of pine wilt disease based on geographic raster variables and machine learning models," *J. Zhejiang A&F Univ.*, vol. 40, no. 3, pp. 617–626, 2023.

[54] B. Xie, J. Cao, J. Xie, F. S. Khan, and Y. Pang, "SED: A simple encoder–decoder for open-vocabulary semantic segmentation," in *Proc. IEEE/CVF Conf. Comput. Vis. Pattern Recognit.*, Jun. 2024, pp. 3426–3436.

[55] S. Zhao, X. Zhang, P. Xiao, and G. He, "Exchanging dual-encoder–decoder: A new strategy for change detection with semantic guidance and spatial localization," *IEEE Trans. Geosci. Remote Sens.*, vol. 61, 2023, Art. no. 4508016, doi: 10.1109/TGRS.2023.3327780.

[56] Q. Wang, H. Rao, and R. He, "Spatiotemporal convolution traffic accident risk prediction based on multi-graph fusion," in *Proc. IEEE 4th Int. Conf. Inf. Technol., Big Data Artif. Intell. (ICIBA)*, Dec. 2024, pp. 962–966.

[57] Z. Zhao, Y. Cao, L. Pei, and Y. Kang, "A spatiotemporal prediction network for vehicle emissions on large road network," in *Proc. IEEE 3rd Int. Conf. Digit. Twins Parallel Intell. (DTPI)*, Nov. 2023, pp. 1–4.

[58] C. Elkan, "The foundations of cost-sensitive learning," in *Proc. Int. Joint Conf. Artif. Intell.*, 2001, vol. 17, no. 1, pp. 973–978.

[59] M. Kerkech, A. Hafiane, and R. Canals, "Vine disease detection in UAV multispectral images using optimized image registration and deep learning segmentation approach," *Comput. Electron. Agricult.*, vol. 174, Jul. 2020, Art. no. 105446.

[60] H. Chen, Y. Chen, and Z. Zhang, "SVRNN: A spatiotemporal prediction model for sea surface temperature prediction in the Taiwan strait," *IEEE Geosci. Remote Sens. Lett.*, vol. 22, pp. 1–5, 2025.

[61] T. Kattenborn, J. Leitloff, F. Schiefer, and S. Hinz, "Review on convolutional neural networks (CNN) in vegetation remote sensing," *ISPRS J. Photogramm. Remote Sens.*, vol. 173, pp. 24–49, Mar. 2021.

Authorized licensed use limited to: University of Chinese Academy of SciencesCAS. Downloaded on March 10,2026 at 08:18:33 UTC from IEEE Xplore. Restrictions apply.